On the Manifestation and Nature of Macroinstabilities in Stirred Vessels

Zacharias Doulgerakis and Michael Yianneskis
Experimental and Computational Laboratory for the Analysis of Turbulence (ECLAT), Div of Engineering King's College London, Strand WC2R 2LS, U.K.

Andrea Ducci
Dept. of Mechanical Engineering, University College London, Torrington Place, WC1E 7JE, U.K.

DOI 10.1002/aic.12519

The flow variations or macroinstabilities (MIs) occurring in a vessel stirred by a pitched blade turbine (PBT) are studied through particle image velocimetry (PIV) experiments. Proper orthogonal decomposition and fast Fourier transform techniques are applied to the PIV velocity data at one vertical and nine horizontal planes below the impeller, to identify and characterize the flow structures present in the vessel. It is shown that the PBT MI is manifested as a precessional movement around the impeller axis and an oscillation in the direction of the axial mean stream around the shaft axis. The identified flow structures are similar to those previously observed in vessels stirred by Rushton impellers and are characterized by two dominant frequencies, equal to one-tenth and one-fifth of the impeller rotational speed. The nature and extent of these structures and their interaction with the trailing vortices emanating from the turbine blades are discussed. © 2011 American Institute of Chemical Engineers *AIChE J,* 57: 2941–2954, 2011

Keywords: mixing, macroinstability, Pitched blade impeller, stirred vessels

Introduction

Fluid mixing processes can be affected by the vortical structures and turbulence levels generated in stirred vessels. Depending on the mixing process considered, the flow patterns and turbulence levels encountered in the mixing vessel can be varied by changing impeller (for example, Rushton and pitched blade turbines that generate mainly radial and axial/mixed flows, respectively) and vessel-impeller configuration, for example, impeller clearance.[1] As a consequence, many studies in the published literature have attempted to characterize the mean flow and vortical structures present in stirred vessels for different vessel-impeller configurations and Reynolds numbers (*Re*). For example, investigations by[2] have shown that mixing in small scales plays an important role, with energy dissipative scales, directly measured by,[3] controlling micromixing efficiency in the impeller stream, while large (whirlpool-like) vortices, denoted as macroinstabilities (MIs), have been shown to enhance macromixing.[4,5]

In the last two decades, the mean velocity and turbulence characteristics of single-phase flows in stirred vessels have been extensively investigated in the impeller region, whereas comparatively little information has been obtained for other locations in the vessel. Recently, an instability manifested as a mean flow variation has received much attention, and it is usually referred to as a macroinstability. Such an instability appears as temporal and spatial fluctuations of the mean flow and has been observed to occur with a frequency well below that of the blade passage. MIs may benefit mixing process operation and efficiency, since such structures can enhance mixing through mean flow variations. For example, the associated low-frequency, high amplitude oscillatory motions have the potential of transporting substances fed to a mixing

---

Additional Supporting Information may be found in the online version of this article.

Correspondence concerning this article should be addressed to A. Ducci at a.ducci@ucl.ac.uk.

process over relatively long distances in regions of low turbulence in a vessel.[6] Furthermore, knowledge of the magnitude and causes of MIs is important: they may affect the time scale of a process, and although the reaction time scale is often shorter than that of the flow motions involved, macromixing will be influenced, making knowledge of the related time scales essential. The potential of MIs for mixing process optimization calls for a more complete understanding of the related phenomena.

The plethora of findings on MIs in vessels stirred by PBT impellers necessitates a comparatively extensive review of the relevant literature. Winardi and Nagase[7] were among the first to study MIs with axial flow impellers. They observed that with a marine propeller at $Re = 48{,}000$ the flow pattern was asymmetric with respect to the impeller shaft. They identified three circulation patterns, the lifetime of each varying from half a second to several minutes. The average lifetime for all flow patterns was 11–16 sec, corresponding to a nondimensional frequency, normalized with the impeller rotational speed, N, of $f' = f/N = 0.0207$–0.029.

Bruha et al.[8] investigated the flow generated by various PBT impellers and they studied the effect of the impeller rotational speed. They observed a vortex that appears as a swelling up of the fluid surface, on a much longer time and length scale than that of the turbulent eddies. They concluded that the frequency of the surface swelling was linearly dependent on N. In a later study (Bruha et al., 1995), using similar impeller and vessel geometries, the linear dependence of MI frequency on N was confirmed and expressed by a relation of the form, $f = k_1 + k_2N$, where $-0.009\text{Hz} \leq k_1 \leq -0.04\text{Hz}$ and $0.041 \leq k_2 \leq 0.05$.

Montes et al.[9] studied PBT MIs in a 300 mm vessel stirred by a 6-bladed 45° PBT ($D = 0.33T$ and $C = 0.35T$, $Re = 380$) and noted no evidence of MIs, while for a slightly larger $Re = 1140$, the MI frequency was quite evident with a value $f' = 0.09$. At higher $Re = 75000$, $f' = 0.0575$ was recorded. They concluded that the MI was a "nonstationary pseudo-periodic phenomenon characterized by a frequency linearly related to the impeller rotational speed." In a similar work with identical vessel and impeller geometries, Hasal et al.[10] applied the proper orthogonal decomposition (POD) technique and they reported almost equal f' values with those of,[9] obtaining $f' = 0.087$ for $Re = 750$ and 1200, and 0.057 for $Re = 75{,}000$.[10] also measured the MI magnitude close to the impeller which was found generally to decrease with increasing Re.

Roussinova et al.[11] investigated PBT MIs for various D and C values, and found that f' value remained constant at 0.186 for $Re \geq 10000$ and for all C values studied, but was slightly higher for lower Re. They concluded that the extent to which the MI persisted throughout the tank and its coherence depend on the impeller and tank size. This work was extended by Roussinova et al.[12] on a larger vessel, but with the same impeller geometry, to study the effect of scaling up on the MIs. The same nondimensional frequency (0.186) was obtained for $Re \geq 20000$, both from experimental results and large eddy simulation predictions, attributed primarily to an impeller jet instability. In a later work, Roussinova et al.[13] utilized two PBT impellers of $D = T/2$ and $T/3$. Their analysis for the small impeller revealed two dominant frequencies. The first was associated to a precessing vortex with frequency $f' = 0.015$, similar to that of Ref. [14] discussed below, and a second one with $f' = 0.065$, which had been previously reported by Bruha et al.[8] For the larger impeller a single resonant frequency of the precessing MI was detected, with the same value as reported in their previous works, $f' = 0.186$. This frequency remained dominant when the off-bottom clearance (C) was changed but was less coherent. Two other less significant frequencies were also noted ($f' = 0.075$ and 0.26) with a distribution of other frequencies around the dominant peaks. The $f' = 0.186$ instability was related to the oscillation of the impeller discharge stream.

Nikiforaki et al.[14] found that with $D = T/3$ and $C = T/3$ impellers the f' value was essentially independent of the impeller design (RT or PBT): the f' of the MI generated by a 60° six-bladed PBT impeller was also in the range of 0.015–0.022 and with both impellers the MI was observed to comprise a precessional motion around the shaft. It should be noted that a second, but equally significant, frequency was observed for the same Re range, with $f' = 0.092$, approximately six times higher than the lower one. Using a 45° PBT, Galletti et al.[15] found that for $13{,}600 \leq Re \leq 54{,}400$ f' values were in range of 0.012–0.028, similar to what the same authors obtained for the RT. Therefore, they concluded that impeller design did not affect the MI frequency, in agreement with the findings of Nikiforaki et al. Galletti et al.[16] reported that with a PBT impeller, but for a different off-bottom clearance ($C = T/4$) and Re range ($Re = 70000$–95000), a dominant peak of $f' = 0.187$ was evident from the frequency analysis, similar to that of the flow instabilities observed by.[12] The energy spectrum obtained from the velocity measurements at $r/T = 0.33$ and $z/T = 0.35$ showed that nondimensional frequencies of 0.02–0.04 similar to Ref. 14 had high energy content, whereas a smaller spectral peak could be identified for $f' = 0.187$.

The preceding review, showed that the flow produced by a PBT impeller is more complex than that of a RT, probably due to the combined axial and radial velocity components induced in the flow by the PBT. This makes identification of the prevailing MI mechanism a more demanding task than is the case with RT and may explain the range of nondimensional frequency values reported in the literature. A variety of macroinstability f' values have been reported, obtained mostly with fast Fourier transform (FFT) techniques, in different locations in the vessels and for a range of Re, impeller designs, diameters and/or clearances, indicating that further study of the flows with PBT impellers is called for to fully understand the dynamics and phenomena involved. There is general agreement that MIs generated by an RT manifest themselves as a precessional flow motion around the impeller shaft. However, for a vessel stirred by a PBT manifestations of the MI as both as precessional and impeller jet instabilities have been reported.[9,14,13]

There are various possible reasons for such different views on the MI nature. First, the differences observed may partly stem from variations in geometry or rotational speed or other such characteristics. Second, as Nikiforaki et al.[14] showed, the sample size employed for the determination of MI frequencies by FFT can strongly affect the dominant peaks observed and deduced from the spectra. Third, the flow generated by a PBT is more complex in that its main direction

Table 1. Vessel and PBT Impeller Dimensions

Vessel		Impeller	
Diameter	$T = 294$ mm	Diameter	$T/2$
Height	T	Blade pitch angle	45°
Baffle width	$T/10$	Blade length	$T/5$
Baffle thickness	$T/100$	Blade thickness	$T/111$
Clearance	$T/2$	Blade height	$T/7.55$

is not perpendicular to the axis of the precessional motion — unlike the RT case — and may thus be subject to less well-defined oscillations. Indeed, Hasal et al.[17] concluded that the MI was of a chaotic nature with different regions of MI dynamics within a tank and noted large scatter in the experimental data, while very recently Roy et al.[18] detected a dominant $f' = 0.2$ in a vessel with a dished-bottom with f' values in different regions in the vessel found to be in the range of previous studies.

In this work, an attempt is made to reconcile the different findings previously reported. The approach employed is threefold. First, the frequencies manifested by FFT analysis over a large region around a PBT impeller are considered in great detail. Second, POD is employed to reveal the main modes of the instability motion and juxtapose it with existing knowledge on the well-defined MIs produced by a RT. Third, extensive PIV/POD data acquired over both horizontal and vertical planes are combined to visualize better the flow variations, in a three-dimensional manner and with more clarity than has been possible hitherto.

The results presented in this article, reveal instability motions and frequencies that exhibit practically all previously reported findings for PBT MIs. It is shown that the complexity of the interactions of the impeller stream generated by a PBT with the precessional MI is a main, if not the, reason why the nature of the PBT MI has so far remained elusive. The combined POD analysis in vertical and horizontal planes provides convincing evidence that the MI manifests itself as a precessional flow motion that instigates an oscillation of the PBT impeller jet.

Flow Configuration and Experimental Apparatus

A transparent cylindrical mixing vessel of diameter $T = 294$ mm ($H = T$), equipped with four equispaced baffles was used to carry out PIV measurements. The experiments were implemented on a vessel stirred by a four blade 45° down-pumping PBT of diameter $D = T/2$, set at a clearance $C = T/2$. The geometric characteristics of the vessel and of the impeller are given in Table 1 and Figure 1. An experimental set up similar to those described in Refs. 19 and 20 was used in this study. A 13 kHz time-resolved 2D Dantec PIV system was employed to illuminate the area of interest, with the camera positioned underneath or at the side of the vessel, depending on whether horizontal or vertical planes of measurement were considered. The working fluid was distilled water seeded with 10μm silver-coated hollow particles. As mentioned in the introduction, the objective of this work was to investigate the characteristics of MI by means of POD to filter out the small scale structures associated to turbulence and separate the large scale ones related to the trailing vortices produced by the PBT impeller. To effectively determine the modes associated to the MI and be able to discard those related to the trailing vortices, two PIV measurement settings were used depending on the vortical structure to be identified, as their characteristic time scales are significantly different. The first one, related to a frame rate of 51 Hz, was optimized to identify the POD modes corresponding to the trailing vortices, whereas the second one with a frame rate of 2 Hz was selected to study MIs. Each data set comprised 1635 instantaneous velocity vector fields. The experiment spatial resolution was 0.025 D, which is comparable to the Taylor length scales directly measured by[3] for the same tank, and high enough to accurately resolve the large scale structures of trailing and MI vortices. Nine horizontal planes located between $z/T = 0.2-0.44$ ($z/T =$ 0.2, 0.25, 0.295, 0.341, 0.386, 0.41, 0.42, 0.43, and 0.44) were investigated (gray color planes in Figure 1), with four of them immediately below the impeller (for $z/T \geq 0.41$), where trailing and MI vortices coexist. The vertical plane was positioned between two adjacent baffles, the bottom edge of the impeller and the shaft axis (blue color plane in Figure 1). For all data sets Re was 28,000 ($N = 1.3$ rps). FFT and POD techniques were mainly used for data post-processing. Given that FFT has been extensively used in the literature and its algorithm is well understood, the following section focuses only on the POD methodology, its characteristics and advantages.

POD and Phase Resolved Analysis

The PIV velocity data were post-processed using the POD method of snapshots. A brief description of the POD technique is provided hereafter, but a more in-depth explanation of the methodology is given by Sirovich[21] and Berkooz et al.[22] POD is a linear technique, based on temporal and spatial correlation analysis, that decomposes a set of signals into a modal base with modes ordered in terms of kinetic energy content. The first modes are the most energetic and associated to large scale structures, such as trailing and MI vortices for a stirred vessel flow, whereas the last ones are

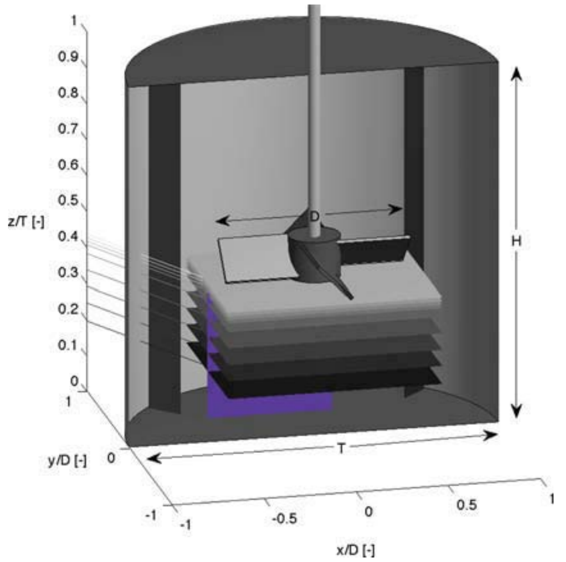

Figure 1. Sketch of the vessel and of the planes where PIV measurements were carried out.

[Color figure can be viewed in the online issue, which is available at wileyonlinelibrary.com.]

the least energetic and related to small scale structures and turbulence. In Eq. 1 the POD analysis is applied to the fluctuating part of the velocity field, $\vec{\mathbf{u}}'$:

$$\begin{aligned}\vec{\mathbf{u}}\left(\vec{x},\ t\right) &= \vec{\mathbf{U}}\left(\vec{\mathbf{x}}\right) + \vec{\mathbf{u}}'\left(\vec{\mathbf{x}},t\right) \\ &= \vec{\mathbf{U}}\left(\vec{\mathbf{x}}\right) + \sum_{n=1}^{N_s} a_n(t)\ \vec{\Phi}_{\mathbf{n}}\left(\vec{\mathbf{x}}\right)\end{aligned} \qquad (1)$$

where $\vec{\mathbf{u}}$ and $\vec{\mathbf{U}}$ are the total and mean velocity flow fields, and $\vec{\Phi}_{\mathbf{n}}$ and a_n are the spatial eigenfunctions and the temporal eigenfunctions (often referred to as temporal coefficients) associated to the *n*th mode, respectively. As already mentioned in the introduction, the main objective of this work is to investigate the MI structures produced by a PBT impeller. From this point of view POD is a useful tool, as it enables to isolate the modes associated to the MI vortices, and low order models, LOM, can be reconstructed from the combination of these modes to best visualize their flow structures by filtering out small scale structures related to turbulence and separating out other large ones, such as trailing vortices, that might interfere with the MI. Similarly to the wake studies of van Oudheusden et al.[23] and Perrin et al.,[24] the large scale structures of the flow under study, trailing and MI vortices, can be captured by POD in pairs of modes, which are locally orthogonal in space and show a periodic variation in time associated to their characteristic frequency. Depending on the number of flow structures of interest and to the level of reconstruction required, a LOM can be recreated from pairs of modes, such as the one of Eq. 2, which is based only on the first two modes.

$$\begin{aligned}\vec{\mathbf{u}}_{\mathrm{LOM}}\left(\vec{\mathbf{x}},\ \phi\right) = \vec{\mathbf{U}}\left(\vec{\mathbf{x}}\right) + a_1(\phi)\ \vec{\Phi}_1\left(\vec{\mathbf{x}}\right)\ldots \\ \ldots + a_2(\phi)\ \vec{\Phi}_2\left(\vec{\mathbf{x}}\right)\end{aligned} \qquad (2)$$

In Eq. 2 the periodic nature of the coherent structures associated to the first two modes is reflected in the sinusoidal variation of the coefficient $a_1(\phi)$ and $a_2(\phi)$ as shown in Eq. 3:

$$a_1(\phi) = \sqrt{2\ \lambda_1}\sin(\phi),\ a_2(\phi) = \sqrt{2\ \lambda_2}\cos(\phi) \qquad (3)$$

The eingenvalue λ_n of Eq. 3 represents the energy content associated to the *n*th mode and its contribution to the total fluctuating energy, and the phase angle ϕ is equal to $\phi = 2\pi ft$, where f is the characteristic frequency of the structure of interest. POD have been successfully applied to stirred vessel flows by Tabib and Joshi,[25] to compare the mixing characteristic of different chemical process equipments, Moreau and Line,[26] to study the flow of RT trailing vortices, and Ducci et al.,[19] to investigate the characteristics of MI produced by a Rushton turbine.

Results and Discussion

The presentation of the results is organized into five subsections. An FFT analysis of the velocity data is given in the following subsection to compare with the results of previous works, as this has been the technique most extensively used to study MIs see, for example, Refs. 11, 16, 27 and 28. The POD analysis is subsequently applied first to data on a horizontal plane located at z/T = 0.2 where only MI frequencies are present, and then it is extended to other horizontal and vertical planes with flow regions affected by the impeller trailing vortices. An attempt to provide a 3D reconstruction of the instability is made in the last subsection.

A considerable amount of data were obtained in this work, but only the most characteristic and relevant data are presented in this section: this selectivity was implemented for brevity of presentation and in relation to data/POD modes that exhibit trends very similar or identical to those shown in Figures 2–14. A complete set of results is provided by Doulgerakis[29] and in the Supporting Information (videos) accompanying this article.

Frequency distribution in horizontal planes of measurement

A frequency analysis of the flow fields in nine horizontal planes, $z/T = 0.2$–0.44, was carried out to determine the flow regions below the impeller dominated by the trailing vortices and by the macroinstabilities. The FFT analysis was applied to 1635 frames of 1178 points in each field of view. The dominant frequencies at each point were identified from the peaks of the FFT of the velocity magnitude, J, defined in Eq. 4. In this way, both the tangential and radial components of the flow were considered. The magnitude of the mean motion was subtracted from the instantaneous fields before applying the FFT.

$$J = \sqrt{(u_\theta)^2 + (u_r)^2} \qquad (4)$$

It has to be stressed that to accurately resolve the energy spectrum in a point and be able to identify local dominant frequencies, the velocity time record must be long enough to include several cycles of the velocity fluctuations to be resolved. This was thoroughly analyzed by Nikiforaki et al.[14] who showed that MI frequency could be accurately resolved from LDA velocity measurements run over a sampling time of 80 times the MI period, T_{MI}. The current PIV settings (frame rate 2Hz) allowed to record 106 and 53 cycles of the *a priori* targeted $0.1N$ and $0.2N$ frequencies, which are mostly encountered in the literature for this *Re*, and therefore should be sufficiently accurate to provide meaningful results over a large area of the flow.

The frequency distribution across the horizontal plane at $z/T = 0.43$ (6 mm below the bottom tip of the impeller blade) is presented in Figure 2(a). To improve the readability of the plot, the dominant frequencies normalized by the impeller rotational speed, N, are associated to five frequency ranges. It is worth noting that one point can be associated to more than one frequency, depending on the number of local peaks exhibited by the FFT. The major conclusion that can be drawn from this figure is that the frequency $f' = 4$, associated to the trailing vortex passage, is dominant within the annulus delimited by $0.3 \leq r/D \leq 0.6$. In the remainder of this work, this frequency will be denoted as f'_{TV}.

The near-circular region of the flow that is not dominated by the trailing vortices, $r/D \leq 0.3$, is characterized by

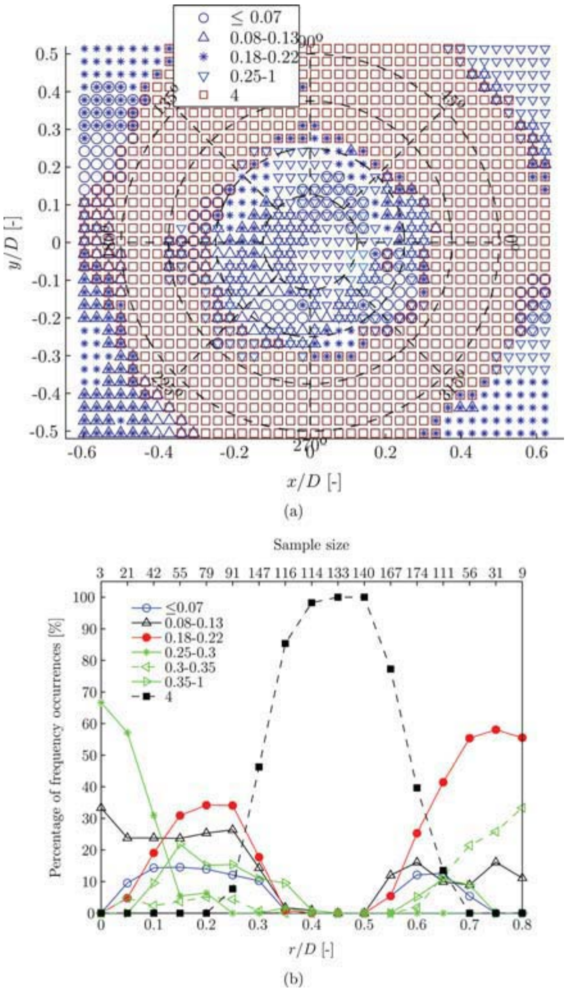

(a)

(b)

Figure 2. (a) Distribution across the plane of measurement of the nondimensional frequency, *f′*, associatd to a local peak in the energy spectrum of the velocity magnitude and (b) Percentage variation of frequency occurrences with *r/D* (*z/T* = 0.43).

[Color figure can be viewed in the online issue, which is available at wileyonlinelibrary.com.]

frequencies lower than 0.25*N*, with the frequency ranges 0.08–0.13*N* and 0.18–0.22*N*, centred around $f' = 0.1$ and 0.2, being dominant. The frequency distribution across the other horizontal planes investigated is not included here for brevity of presentation, but it is worth to mention that a similar distribution to that displayed in Figure 2a was found, with the annular region dominated by the trailing vortices shrinking in size and the inner circle, associated to low frequency ranges, becoming larger as axial locations further away from the impeller were considered. The influence of the trailing vortices on the local flow becomes small at $z/T = 0.386$ and no evidence of their presence was observed at $z/T = 0.341$. Schäfer et al.[30] showed that at an azimuthal plane of $r/T = 0.164$, the trailing vortices extend to $z/T = 0.23$, over a distance of 0.133*T* from the impeller. Given the larger impeller, employed in this work, their results are consistent with those presented in this study, where the trailing vortices were found to extend over an axial distance of around 0.163*T*. The consistent presence of the frequency ranges related to $f' = 0.1$ and 0.2 within the inner circles of increasing size for decreasing *z/T* might imply that MIs originate below the impeller and evolve into more-coherent structures at lower positions where trailing vortex effects start to fade.

A more effective method to present the frequency distribution shown in Figure 2a is provided in Figure 2b, where the percentage of occurrences of different frequencies within the ranges previously defined is plotted as a function of the radial distance *r/D* for the horizontal plane $z/T = 0.43$. The number of points considered at each radial distance is reported on the horizontal axis at the top of the figure. The sample size should be taken into account in the analysis of Figure 2b, as the number of locations for a given *r/D* is statistically relevant for $0.1 < r/D < 0.75$, with radial coordinates outside of this range being associated to sample sizes lower than 40. As expected, trailing vortices dominate the area $0.3 \leq r/D \leq 0.6$ (black dashed line with squares) with a maximum frequency occurrence of 100% at $r/D = 0.45$. As discussed in Figure 2a, the frequency ranges related to $f' = 0.1$ and 0.2 are significant for $r/D < 0.3$, with maxima of frequency occurrence of 25% and 35%, respectively. From this point of view, it should be remarked that nearly 75% of the frequency values included in the range $f' = 0.08-0.13$ are associated to 0.1*N*, which has been consistently reported in the literature for a PBT impeller.[10,11,12,14,16,27,28] In addition, frequencies within the range of 0.18–0.22*N*, are also present for $r/D \geq 0.65$.

Similar analyses to that of Figure 2b were made for lower horizontal planes both in proximity, $z/T = 0.381$–0.42, and away, $z/T \leq 0.341$, from the impeller. The major findings that were made from the analysis of these plots, which are not included in the current work for brevity of presentation, are reported hereafter and for a more detailed analysis the reader is referred to Ref. 29. As mentioned earlier the annular region subject to a higher incidence of the trailing vortex frequency, $f'_{TV} = 4$, decreases in size with decreasing elevation with the range of radial coordinate of the annulus varying from $r/D = 0.2$–0.7 for $z/T = 0.43-0.44$ to $r/D = 0.4-0.7$ at $z/T = 0.386$, which is the lowest axial coordinate investigated where f′tv occurred. Furthermore the peak of f'_{TV} occurrence decreased from 100% to 70% with decreasing *z/T*, while the associated radial coordinate, *r/D*, increased from 0.4 to 0.55 at $z/T = 0.44$ and $z/T = 0.386$, respectively. When horizontal planes with $z/T \leq 0.341$ were considered, the three frequency ranges corresponding to mean frequencies of $f' = 0.04$, 0105, and 0.2 were found to be prevalent with a cumulative occurrence up to 90% of the total number of points considered in each plane.

Phase resolved POD applied to the horizontal plane z/T = 0.2

In this section, the POD results for the horizontal plane positioned at $z/T = 0.2$ are presented. In Figure 3, the proportion of the energy associated to the first 12 POD modes is shown. The results presented in this figure take into account the kinetic energy of the fluctuating part of the velocity, $\vec{\mathbf{u}}'$, as the mean motion has been removed before

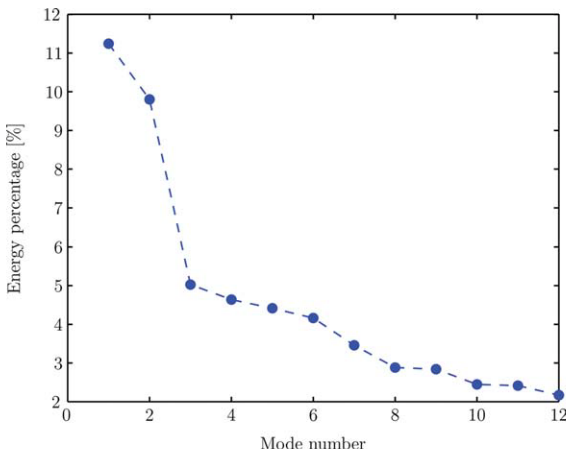

Figure 3. Percentage of energy associated to each mode (*z/T* = 0.2).

[Color figure can be viewed in the online issue, which is available at wileyonlinelibrary.com.]

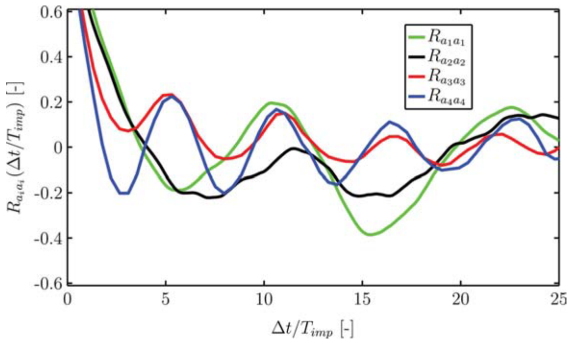

Figure 4. Plot of the autocorrelation coefficient of the temporal eigenfunctions a_1, a_2, a_3, and a_4 associated to modes 1, 2, 3, and 4 (*z/T* = 0.2).

[Color figure can be viewed in the online issue, which is available at wileyonlinelibrary.com.]

applying the POD according to Eq. 1. The energy content is rapidly decreasing when considering higher modes (i.e., smaller flow structures), with the first two modes containing up to 21% of the total energy of the flow in this plane.

A frequency estimation related to the first four modes can be made by carrying out an autocorrelation analysis (for $i = j$) for each a_i coefficient, according to Eq. 5 see[4]:

$$R_{a_ia_j}(t_0, \Delta t) = \frac{\overline{a_i(t_0)a_j(t_0+\Delta t)}}{a'_i(t_0)a'_j(t_0+\Delta t)} \qquad (5)$$

The fluctuation of the autocorrelation coefficients, a_1, a_2, a_3, and a_4 with respect to $\Delta t/T_{\mathrm{imp}}$, is shown in Figure 4, where T_{imp} is the period of an impeller revolution. The first two coefficients (green and black lines) oscillate with a period of $\sim$10 T_{imp}, associated to a nondimensional frequency $f' = 0.1$. Similarly the temporal coefficients corresponding to modes 3 and 4, a_3 and a_4 (red and blue lines), fluctuate with a period of 5 T_{imp} (i.e., $f' = 0.2$). From Figure 4, it can be concluded that in this plane the flow produced by a PBT is characterized by two fluctuating structures/instabilities with nondimensional frequencies of $f' = 0.1$ and $f' = 0.2$, respectively. These results are in agreement with those presented in the previous section, but it has to be stressed that in this case the MI frequencies are better defined and identifiable from the autocorrelation as well as from the FFT of the temporal coefficients, $a_n(t)$, because POD takes into account the variation in time of the velocity in all the points of the region investigated and not just the time series from a single location. In this way large scale fluctuations of the flow field associated to a specific characteristic frequency can be more effectively extracted from the original data. As reported in the introduction similar frequencies were also measured by Paglianti et al.,[31] who investigated the flow in a vessel stirred by a four blade PBT of diameter $D = T/2.5$ at $C = T/3$ and identified a dominant low frequency of $f' = 0.1$ across the vessel, and Roussinova et al.,[12,13] who reported a frequency similar to the second one, $f' = 0.2$, for a slightly smaller tank, $T = 0.24$ m, but with same impeller characteristics and clearance. It should be stressed that according to[13] the off-bottom clearance, C, has a negligible effect on the MI frequency.

The phase-resolved averages of the first four coefficients, a_1, a_2, a_3, and a_4, nondimensionalized with the velocity of the blade tip, V_{tip}, are shown in Figure 5. The 90° phase difference between the pair of coefficients a_1 and a_2 (green and black lines) is evident, which confirms the temporal orthogonality between the first two modes. Similarly, the second pair of coefficients, a_3 and a_4 (red and blue lines), associated to modes 3 and 4, are also out of phase by 90°, and thus are also orthogonal to each other. It should be noted that the amplitudes of the fluctuations of the first and the second pair of coefficients are of the same order of magnitude, implying that the contribution of the second pair of modes to the local flow at $z/T = 0.2$ is relevant and should not be discarded.

The vorticity contours together with the corresponding flow patterns of the spatial eigenfunctions $\vec{\Phi}$ associated to modes 1, 2, 3 and 4 are shown in Figures 6a–d, respectively.

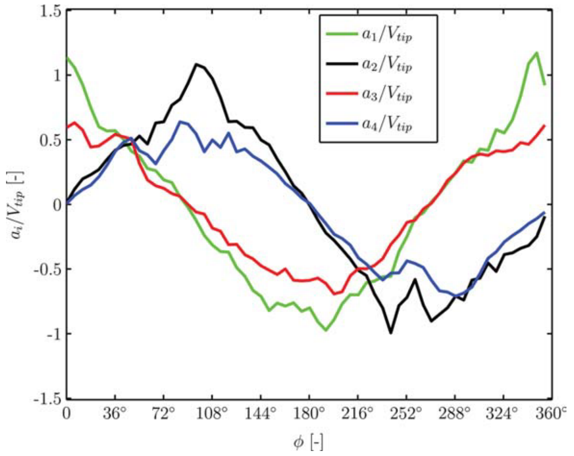

Figure 5. Variation of the phase-resolved temporal coefficients a_1, a_2, a_3, and a_4 normalized with V_{tip}, with MI phase angle, ϕ; (*z/T* = 0.2).

[Color figure can be viewed in the online issue, which is available at wileyonlinelibrary.com.]

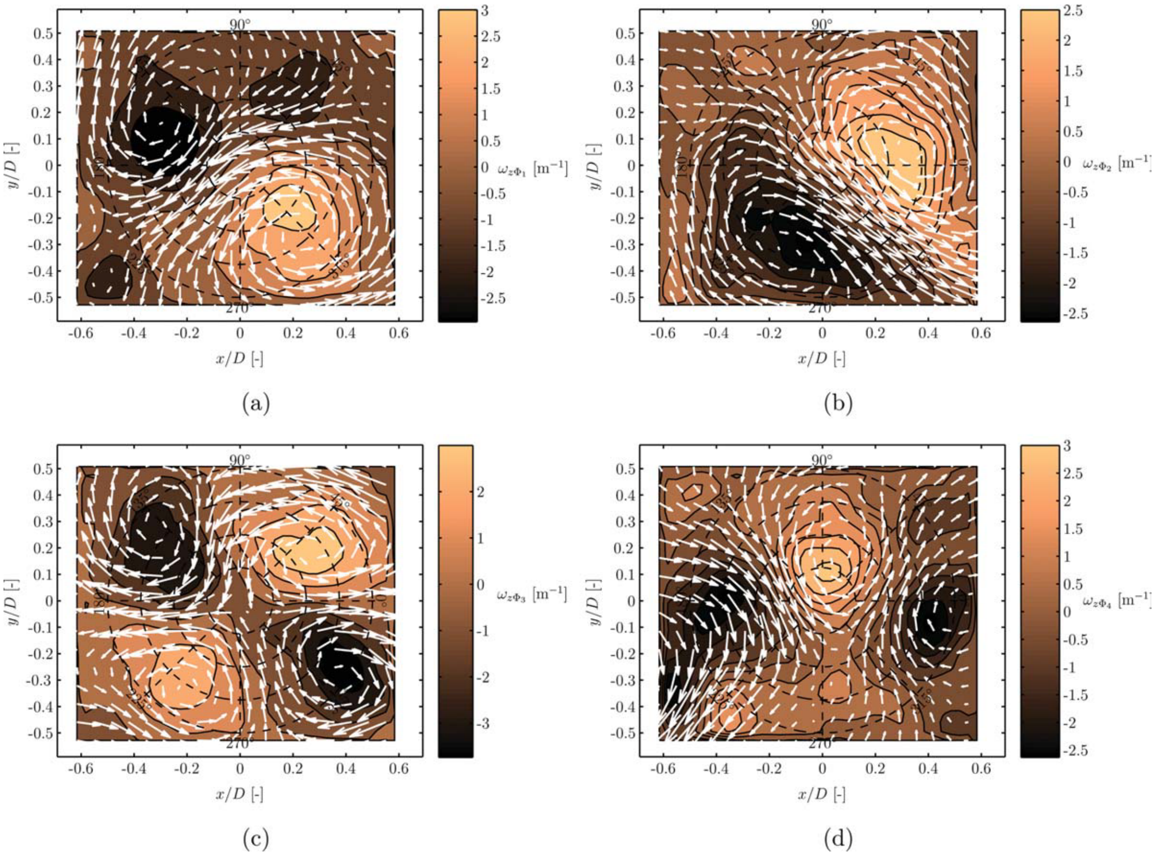

Figure 6. Plot of the velocity field and contours of the vorticity associated to: (a) Mode 1; (b) Mode 2; (c) Mode 3; (d) Mode 4 (z/T = 0.2 and Re = 28000).

[Color figure can be viewed in the online issue, which is available at wileyonlinelibrary.com.]

From Figures 6a,b, it is evident that the flow structures of modes 1 and 2 ($f' = 0.1$) are related to each other, as they both exhibit two distinct regions of negative and positive vorticity which are offset by 90° in the tangential direction θ. This is in agreement with the findings of[23] for a cylinder wake flow, who reported that the flow patterns associated to the first two modes are shifted in the convective direction of the flow. In the present study the flow is rotational and therefore the convective direction is θ. Similarly, the flow patterns of modes 3 and 4 ($f' = 0.2$) shown in Figures 6c,d, are analogous, with an hyperbolic kind of flow pattern and two pairs of opposite regions of positive and negative vorticity. In this case, the two modes are shifted along the tangential direction by 45°. It should be stressed that the contours of $\omega_{z\Phi_n}$ (i.e., $\frac{\partial \Phi_{ny}}{\partial x} - \frac{\partial \Phi_{nx}}{\partial y}$) provide only a qualitative indication of size and shape of the flow structure associated to the nth mode, and their intensity is dimensionally meaningful only when multiplied by the corresponding eigenfunction $a_n(t)$.

The flow patterns of the the first and second pair of modes of the current flow are similar to those studied by Ducci et al.,[19] in a vessel stirred by a Rushton turbine of smaller diameter ($D = T/3$) and for Re = 27200. Similarly to Ducci et al.,[19] the MI structure associated to the LOM of the first two modes (Figures 6a, and b) can be seen as a radial off-center perturbation of the mean flow, that results in a precession of the vortex core centre around the impeller axis with a nondimensional frequency of 0.1. The LOM of the second pair of modes, 3 and 4 (Figures 6c, and d), describes an instability that stretches/squeezes the vortex core along a direction that is rotating with a nondimensional frequency of 0.2 around the vortex axis. The LOMs associated to the high and low frequency instabilities identified above are not included here for brevity of presentation, as their dynamics are very similar to those exhaustively reported in Ref. 19.

To obtain a better understanding of the differences and similarities between the flow instabilities produced by the two impellers, the spatial modes associated to the PBT and the RT ($D = T/3$) impellers are presented in Figure 7, together with the corresponding frequencies, for Re = 28,000 and 27,200, respectively. From Figure 7, it is evident that not only the flow patterns associated to the two pairs of modes are very similar for both the impellers considered, but also the lower frequency, always associated to the off-centering instability, is half that corresponding to the squeezing/stretching instability, irrespective of the impeller design and size. From the above considerations and literature analysis three major conclusions can be made on physical mechanisms underlying macro-instability phenomena in stirred tanks: (i) the rotational nature of the flow produced by an impeller induces a flow below the impeller that is precessional in essence and can be seen as an off-centering instability of the mean flow; (ii) A squeezing/stretching perturbation of the mean flow is also present and its intensity and

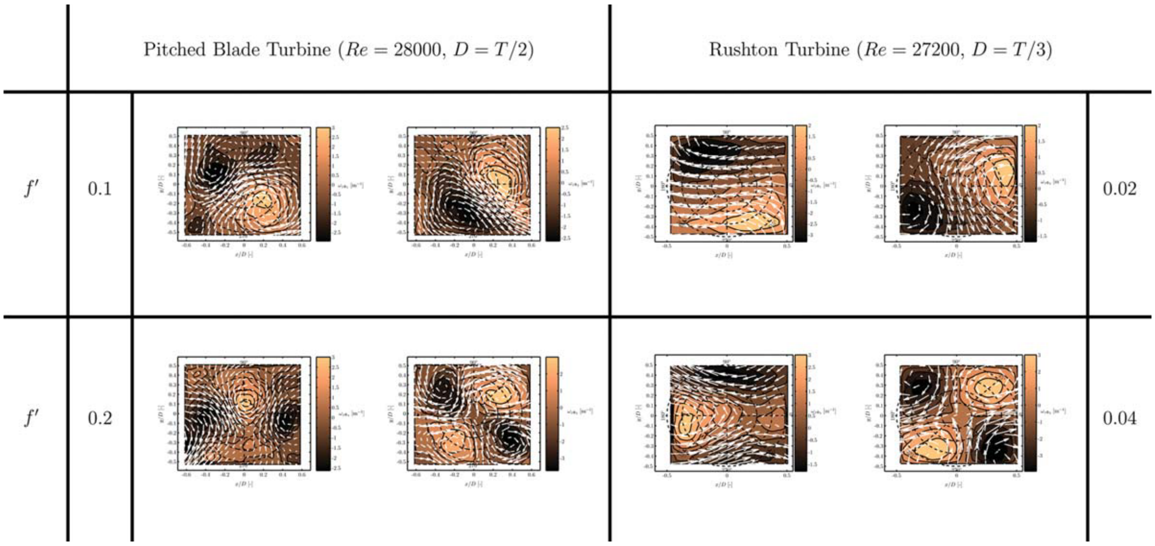

Figure 7. Comparison between the off-centering and squeezing/stretching modes, which are extracted by POD for flows produced by PBT and RT.

[Color figure can be viewed in the online issue, which is available at wileyonlinelibrary.com.]

impact on the total flow might differ depending on *Re* and on the impeller employed; (iii) The characteristic frequencies of the two perturbations/instabilities are affected by the impeller design and Re/rotational speed.

The above observations do not explain so far the impeller jet instability reported previously: this issue is addressed later through the considerations made from the vertical plane measurements.

MI spatial modes for horizontal planes at $z/T = 0.2$–0.44

The POD analysis was applied to all horizontal planes of measurements, to assess whether the MI flow structures identified in the previous section for $z/T = 0.2$ were consistently present in regions closer to the impeller, where trailing vortices dominate the local flow. When the POD analysis was implemented over the entire camera field of view ($\approx D \times D$), the flow structures associated to the trailing vortices could be identified effectively with pairs of modes uniquely associated to a frequency $f'_{TV} = 4$. However, this approach proved to be less efficient in identifying the modes related to the frequencies $f' = 0.1$ and 0.2, which were clearly determined with the single-point-FFT analysis already discussed in relation to Figure 2. The reason for this is that, in regions where the trailing vortices are present, their energy content may dominate locally the structures associated to modes 1 and 2, even though MI-related structures may be evident for the higher modes 3 and 4. The flow structures are complex in such regions, and it is difficult or not possible to distinguish MI modes over a region where, there is a strong influence of the trailing vortices.

It was thus decided to limit the application of POD to the inner circles associated to $f' = 0.1$ and 0.2, which were identified for each plane of measurement from the single-point-FFT analysis. For example, the POD analysis for the plane at $z/T = 0.43$ was limited to a circle with $r/D \leq 0.3$ (see Figure 2a). This approach proved to be very effective and the velocity fields and vorticity contours of the first mode, consistently related to a nondimensional frequency $f' = 0.1$, are shown in Figure 8 for all the horizontal planes investigated. In agreement with the findings related to $z/T = 0.2$ (bottom plane in Figure 8) the first mode exhibits two areas of opposite vorticity for all the planes considered. A similar structure was identified for mode 2, whereas modes 3 and 4 were characterized by the hyperbolic flow pattern already described above. The flow fields of the three highest planes considered, $z/T = 0.44$, 0.41, and 0.386, were characterized mainly by a central radial stream, which rotated with a frequency of $f' = 0.1$ when the first two modes are combined in a low order model, and the two counter-rotating circulation patterns were not as evident as at $z/T = 0.2$. This might be explained by considering that POD was limited to a small part of the entire field of view and the PIV resolution might not have been sufficiently high to fully resolve such structures.

When comparing the data at different planes (Figure 8), it appears that the modes are off-set in the tangential direction, with the negative vorticity region being located at a different tangential coordinate around the impeller axis. This lack of alignment is artificial as it should be recalled that these flow structures rotate around the impeller axis and the measurements from which the different modes are plotted in the figure were not synchronized.

While the shape and dynamics of the modes remains the same, their size increases with decreasing elevation, to extend nearly over the entire field of view at $z/T = 0.2$. The last consideration is directly related to the fact that the influence of the trailing vortices on the local flow diminishes with increasing distance from the impeller and MIs can spread out in the radial direction over a larger area. This is well represented in the sketch of Figure 9, where the gray area affected by MIs is confined in a conical region delimited by the trailing vortices. In Figure 9, the MI vortex axis is indicated by black squares.

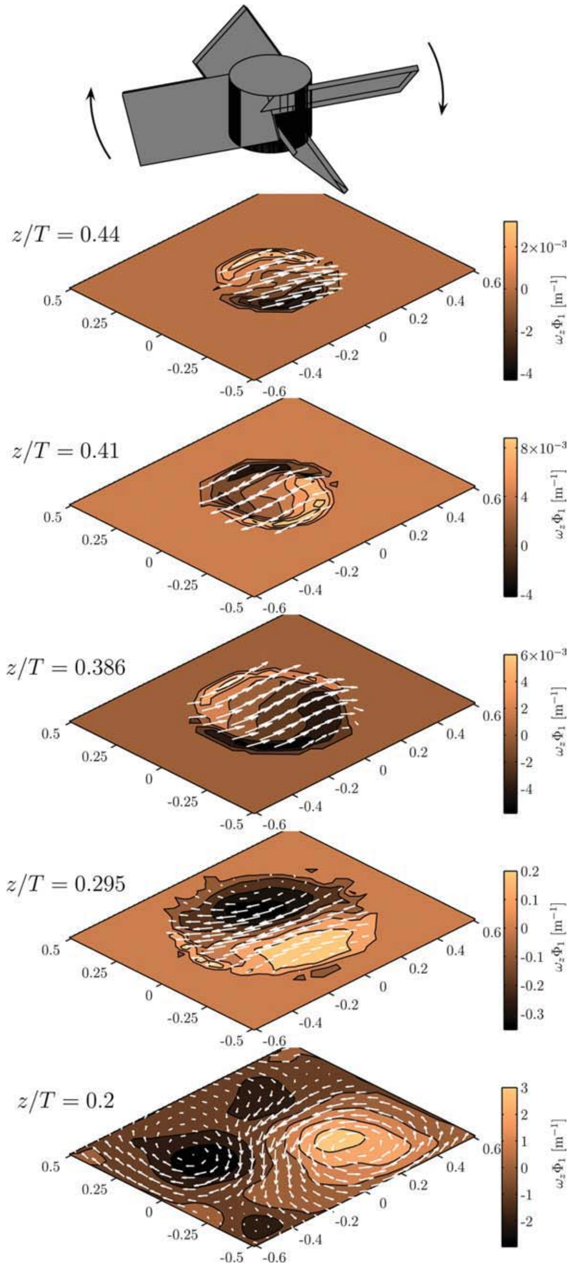

Figure 8. Plots of the velocity fields and vorticity contours of the first spatial mode at five axial locations, *z/T* = 0.2−0.44.

[Color figure can be viewed in the online issue, which is available at wileyonlinelibrary.com.]

Vertical plane measurements

The results of the PIV experiments carried out in a vertical plane are discussed in this section. The measurements on the vertical plane were made for three reasons: first, to validate the findings related to the horizontal planes, second, to determine the effect of the MIs on the axial velocity component. Third, to obtain a description of the flow in the plane in which the impeller jet is clearly in evidence, and thus to investigate the presence of instabilities of this jet such as that reported by Roussinova et al.[12]

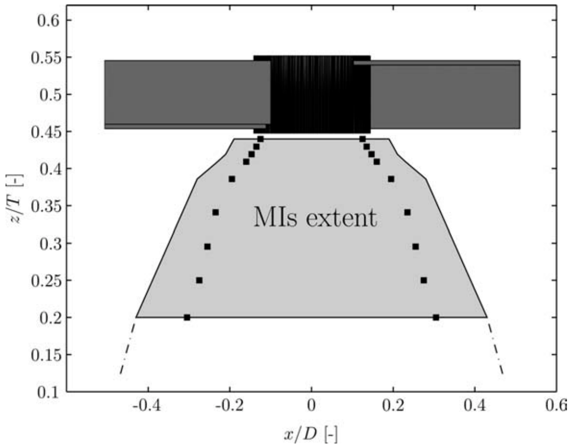

Figure 9. Sketch of the region (light gray) below the impeller that is directly influenced by MI structures.

■, Radial position of the MI vortex center at different elevations, *z/T*.

Prior to applying the POD methodology, the single-point-FFT analysis previously employed was also applied to the vertical plane PIV measurements. The FFT was made from the local velocity magnitude, *J*, obtained from the axial and radial components. The distribution across the vertical plane of the frequencies associated to a peak in the local energy spectrum is presented in Figure 10. To be consistent with the results of Figure 2a the peak frequencies were associated

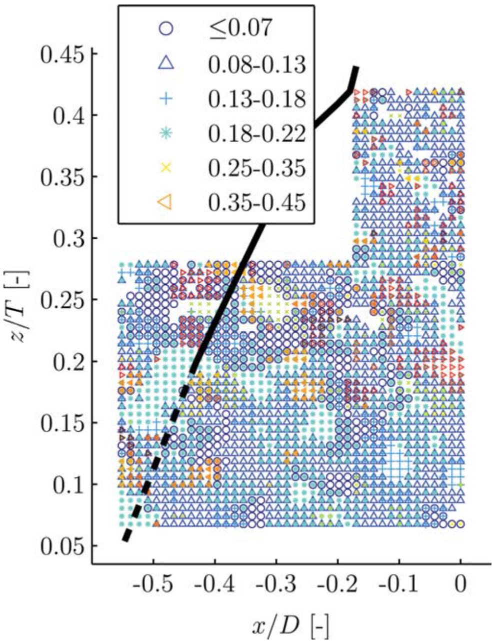

Figure 10. Distribution across the plane of measurement of the nondimensional frequency, *f′*, associated to a local peak in the energy spectrum of the velocity magnitude (Vertical plane, *Re* = 28000).

[Color figure can be viewed in the online issue, which is available at wileyonlinelibrary.com.]

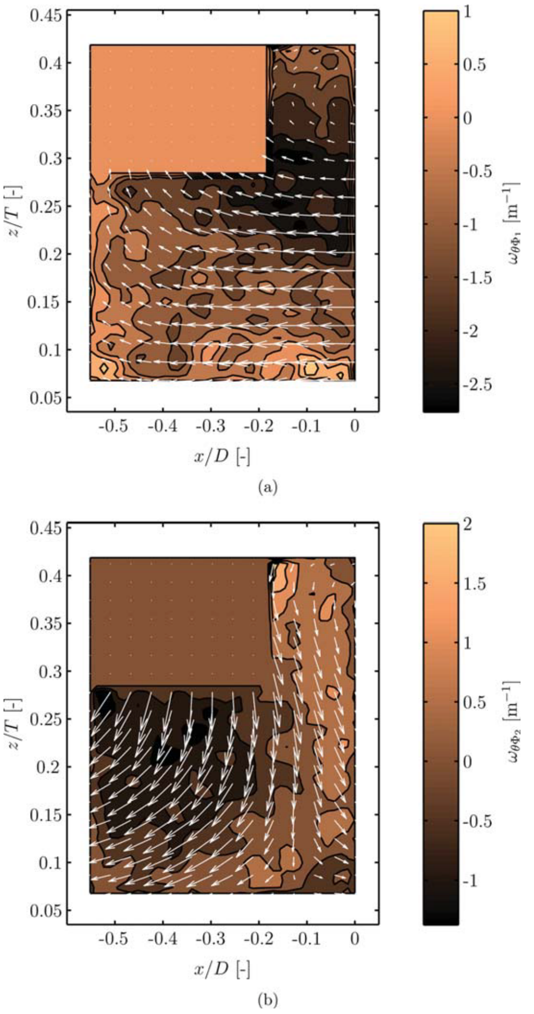

Figure 11. Plots of the velocity field and contours of the vorticity of the MI associated to: (a) Mode 1; (b) Mode 2 (Vertical plane, *Re* = 28000).

[Color figure can be viewed in the online issue, which is available at wileyonlinelibrary.com.]

to the six frequency ranges defined for the horizontal plane data, where it was found that frequencies of $f' = 0.1$ and 0.2 occurred more frequently with a percentage of 30 to 50% of the total points considered, depending on the horizontal plane investigated. The vertical plane measurements confirm these results, with the frequency ranges $0.08 \leq f' \leq 0.13$ (triangles, Δ) and $0.18 \leq f' \leq 0.22$ (asterisks, *) occurring in 60% and 50% of the total number of points considered, respectively. It should also be noted that the frequency $f' = 0.1$ accounts for up to 80% of the total peak frequencies included in the range $0.08 \leq f' \leq 0.13$, while $f' = 0.2$ occurs in 65% of the frequency realisations associated to the range $0.18 \leq f' \leq 0.22$. In agreement with the results of the previous section, the results of Figure 10 show that the radial distance over which $f' = 0.1$ is dominant varies with z/T. Close to the impeller, where the trailing vortices are stronger (the omitted square area in the top-left corner of Figure 10), the region characterized by higher occurrence of $f' = 0.1$ is limited to $-0.18 \leq x/D \leq 0$. With decreasing elevation, for example at $z/T = 0.2$, the frequency of $f' = 0.1$ is found over a greater radial range, $-0.43 \leq x/D \leq 0$, while further below it occurs almost over the entire radial range investigated.

The previous considerations support the conclusions previously made, where it was found that the significance of the frequency $f' = 0.1$ increases with decreasing elevation. To compare the results obtained from the vertical and horizontal planes, the boundaries of the MIs region obtained from the horizontal plane measurements are superimposed with a black line on the vertical plane data of Figure 10. The boundaries have been linearly extrapolated for $z/T \leq 0.2$, which was the lowest horizontal plane investigated. The agreement between the two sets of experiment is reasonable with the area dominated by MIs being associated mostly with frequencies in the 0.08–0.13 range.

The velocity fields and vorticity contours of the first two spatial eigenfunctions associated to the two highest energetic modes of the vertical plane data are presented in Figures 11a,b, respectively. Similarly to the analysis carried out in the previous section, the POD analysis was applied to the central part of the plane, excluding the square region in the top-left corner of the plot, which is most directly influenced by the TV. The velocity fields of modes 1 and 2 are both characterized by a large region of negative radial vorticity and are locally orthogonal to each other. In agreement with the FFT analysis previuosly described the temporal eigenfunctions of the first two modes were characterized by a frequency $f' = 0.1$.

The flow pattern and vorticity contours of the mean flow are shown in Figure 12, where the flow field indicates an upward axial flow. This characteristic is linked to the inner part of the circulation loop created by the impeller discharge jet, which impinges on the wall, moves downwards and returns towards the impeller. Similar findings were also obtained by Jaworski et al.,[32] who studied the flow generated by a six blade 45° PBT impeller (C and $D = T/2$, $Re =$ 34,000), with LDA measurements and CFD predictions. A

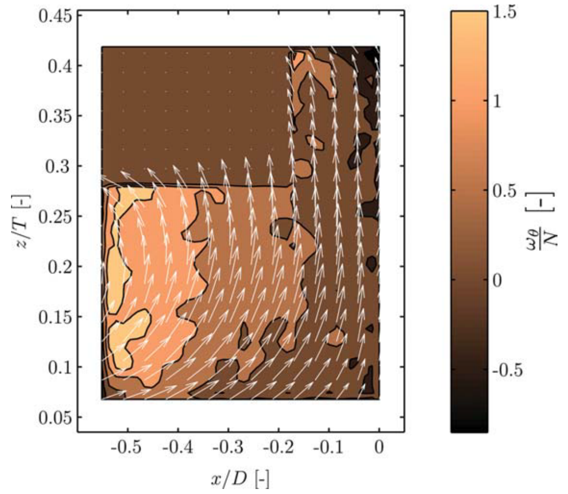

Figure 12. Vector plot of the mean flow pattern and contour plot of the dimensionless vorticity associated to the mean motion (Vertical plane, *Re* = 28000).

[Color figure can be viewed in the online issue, which is available at wileyonlinelibrary.com.]

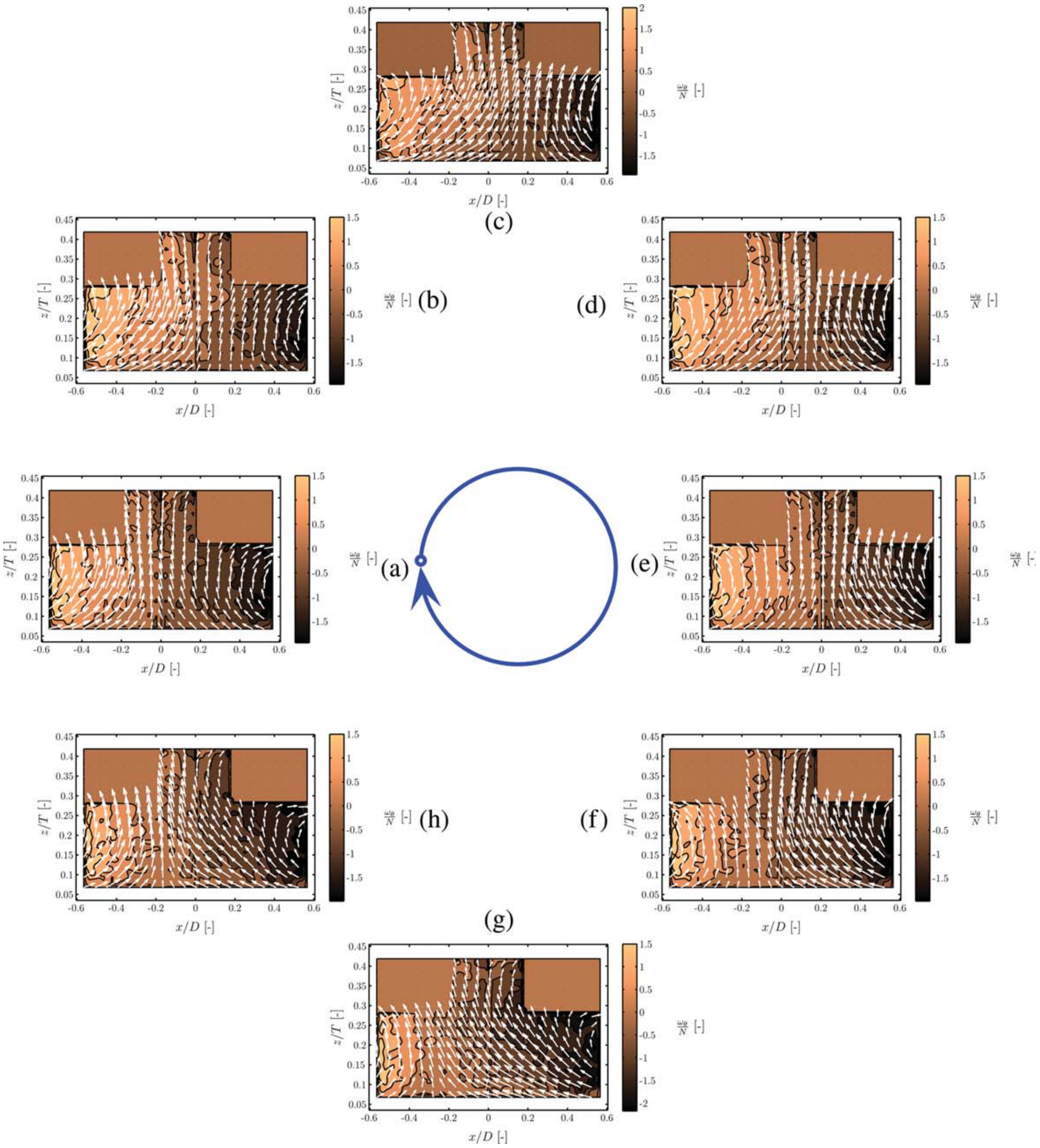

Figure 13. Vector plots of the superimposed LOM and contours of the corresponding dimensionless vorticity for eight values of ϕ: (a) $\phi = 0°$; (b) $\phi = 45°$; (c) $\phi = 90°$; (d) $\phi = 135°$; (e) $\phi = 180°$; (f) $\phi = 225°$; (g) $\phi = 270°$; (h) $\phi = 315°$; (Vertical plane, *Re* = 28000).

[Color figure can be viewed in the online issue, which is available at wileyonlinelibrary.com.]

more effective visualization of the flow underneath the impeller can be obtained by mirroring the vertical measurement data around the impeller axis for $r/D \geq 0$.

Based on the above consideration, the vorticity contours together with the corresponding flow patterns of the LOM obtained from the superimposition of the mean flow and the first two modes are shown in Figure 13a–h, for eight angles of ϕ, over an area centered around the tank axis ($-0.55 \leq x/D \leq 0.55$). The flow associated to the combination of modes 1 and 2 was assumed to be out of phase by $\phi = 180°$ between regions with $x/D \leq 0$ and $x/D \geq 0$, which were directly measured and indirectly estimated, respectively. The vorticity contours show two counter rotating regions of positive and negative vorticity located at the left and right side of the plane, respectively, with a zone of almost zero vorticity present in the central region, underneath the impeller hub ($x/D = 0$). The two opposite regions of positive and negative vorticity alternatively grow or decrease in size depending on the ϕ considered. For $\phi = 0°$ (Figure 13a), a strong axial stream aligned with the shaft axis is formed, while simultaneously the zero vorticity region is suppressed around the shaft axis. With increasing phase angle, $\phi = 45°$ and $90°$ (Figures 13b, c, respectively), the axial stream starts showing a positive radial component (inclined at around 45° to the right), whereas the area of positive vorticity also expands along the

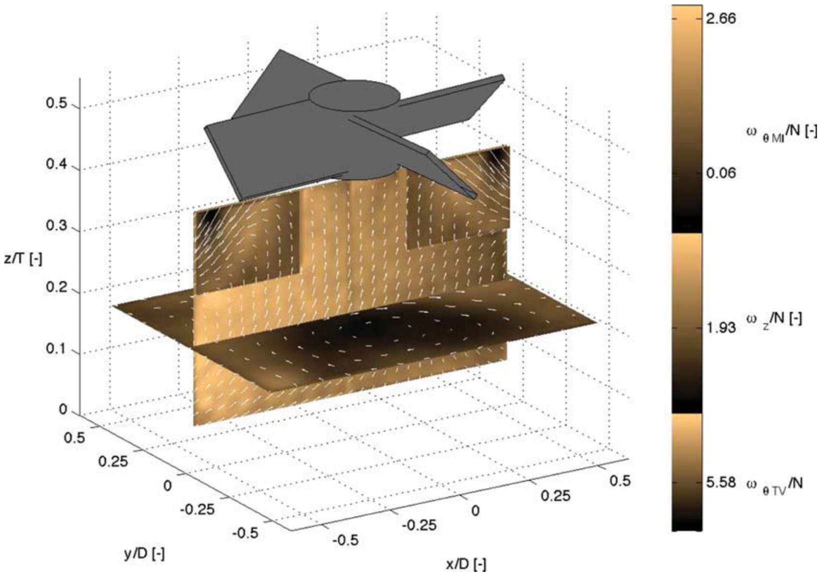

Figure 14. Vector plot of the superimposed LOM and contour of the corresponding dimensionless vorticity for $\phi = 90°$; (data both from the vertical and horizontal planes).

[Color figure can be viewed in the online issue, which is available at wileyonlinelibrary.com.]

radial direction, by squeezing the negative vorticity region on the left side of the plane. As the phase angle is further increased to 180° and 270° (Figures 13e and g, respectively), the flow initially returns to its original vertical position and thereafter it turns to the opposite direction than that of Figure 13c (inclined at around 45° to the left), before completing a MI cycle.

A closer look to the vorticity contours, for example at 270° (Figure 13g), can provide some information of the size of the area, which is affected by MI. The region denoted by a vorticity level $|\omega| \leq 0.5$ below the impeller, at $z/T = 0.42$, is spread over a cylindrical area of radius $|x/D| \approx 0.2$. As the elevation is decreased, the area occupied by the MI increases in radius, and for example at $z/T = 0.2$, it occupies a region of radius $\sim|x/D| \approx 0.43$.

To better visualize the oscillating axial stream, the results of Figure 13 are presented in the accompanying video Supporting Information (filename: vertical.avi, Codec ID: png) of a total duration of 7.7 seconds. The Supporting Information video contains a full MI precession, and its length corresponds to the actual period of the MI.

Combination of vertical and horizontal plane data

The previous findings can be summarized as follows. The vertical plane measurements show the presence of an axial stream, which oscillates in the radial direction from one side to the other with a frequency $f' = 0.1$. The results of the vertical plane are in good agreement with those of the horizontal planes showing that the MIs affect an area of increasing radius when moving in the axial direction away from the impeller. From these considerations, it can be concluded that both the vertical and horizontal planes provide a comprehensive description of the same instability, which is associated to two simultaneous motions: (a) a precessional movement around the impeller axis and (b) an oscillation in the direction of the axial mean stream around the shaft axis.

To visualize better the three dimensional effect of these motions, the results of the vertical and horizontal ($z/T = 0.2$) planes are combined in the velocity vector and vorticity contours plots shown in Figure 14 for $\phi = 90°$. The LOM associated to the trailing vortices is also shown in the upper left and right regions of Figure 14. The exact position of the impeller in relation to the trailing vortices was determined by comparing the current data with the results of Schäfer et al.,[30] who analysed the trailing structure of a 45° PBT impeller in depth. It should be noted that the velocity vectors of the trailing vortex area are not scaled with the vectors over the rest of the planes (vertical and horizontal), as the trailing vortex velocity is much higher than that of the MI, and if they were plotted with the same scale the vectors over the other planes would not be visible. This is also evident from the vorticity levels ($\omega_{\theta TV}$) of the LOM of the trailing vortices, which are ~10 times higher than those of the MI of the vertical plane ($\omega_{\theta \mathrm{MI}}$). It should be noted that the vorticity levels of the two planes are plotted on the same colorbar, with the vorticity of the horizontal plane denoted as ω_z, whereas that of the vertical one as $\omega_{\theta MI}$ for the MI, and $\omega_{\theta TV}$ for the trailing vortex regions.

A complete visualization of the 3D MI flow is given in the Supporting Information video (filename: 3D.avi, Codec ID: png) with a total duration of 7.7 seconds. The Supporting Information video contains a full MI precession, and its duration corresponds to the actual period of the MI. The Supporting Information video is also available in a slower version (filename: 3Dlong.avi, 30 seconds, Codec ID: png), in order for the reader to better visualize the phenomena that are taking place during the MI period. As the MI precesses around the vessel axis, the movements described in the previous section are evident, with the precessing instability displayed on the horizontal plane (darker area) and the oscillating axial stream on the vertical one. The flow fields on the two planes were syncronized by using the radial velocity components of the two data-sets along the line of intersection between the planes. To fully understand this mutual activity, the reader is advised to follow the MI on the horizontal plane and consider the combination of the vectors associated to the horizontal plane, with those of the vertical one at the intersection of the two planes. In the beginning of the Supporting Information video, the MI is located at $\approx 20^\circ$ from the line defined by the intersection of the two planes and rotating clockwise, while the velocity vectors of the vertical plane are pointing to the left, in agreement with the direction of movement of the MI. As the MI moves towards the second quadrant (front side of the horizontal plane), the velocity vectors close to the line of intersection between the planes start pointing to the right, in agreement with those of the vertical plane.

The observations made possible from the combination of all PIV/POD data shown above, allow an additional, fourth conclusion to the three major findings on the nature and manifestation of the MIs given above for the horizontal plane data at $z/T = 0.2$, to be made: the precessional perturbation of the mean flow manifests itself in vertical planes as an oscillation of the circulation loop formed by the impeller jet below the PBT.

Conclusions

In this work, the macroinstabilities present in a vessel stirred by a PBT were studied with POD analysis applied to PIV velocity data for various horizontal planes and one vertical plane below the impeller. A range of instability frequencies were detected that include practically all previously reported f' values. Only two of these frequencies were most significant in locations where the trailing vortices are not dominant. POD analysis of the data over an area of radius $|x/D| \leq 0.23$ for the highest elevation plane considered ($z/T = 0.44$), revealed the same two patterns as those obtained for the lowest plane investigated ($z/T = 0.2$). The first, with $f' = 0.1$, accelerated the solid body rotation on the one side, and attenuated it on the other. The second, with $f' = 0.2$, elongated/squeezed the flow structures. The analysis showed that the dynamics that governs the flow generated by a PBT, although they exhibit different frequencies, are similar to those occurring in a vessel stirred by a RT, with the higher frequency f' being exactly double than the the lower one for both cases. Visualization of the flow via a combination of the data in both vertical and horizontal planes showed that the resulting instability of the flow in the vessel stirred by a PBT manifests itself as a precessional motion around the impeller shaft that induces an oscillation of the impeller jet in the radial direction.

FFT analysis of the velocity data showed that the frequency distribution of the MI and trailing vortex structures produced by a PBT impeller is rather complex, but comprising two main regions: an outer region, which was found to be dominated by the trailing vortices and an inner region characterized by frequencies with $f' \leq 0.25$. With decreasing elevation, the radius of the inner region increased to reach a value of $|x/D| = 0.43$ at the lowest horizontal plane investigated and the two frequency ranges with values around $f' = 0.1$ and 0.2 became more dominant. The area dominated by the macroinstabilities was thus shown to comprise a conical region below the impeller.

Clearly, the present data, although extensive, were obtained only under the impeller, primarily as optical access was more readily available there; however, due to the geometric symmetry of the arrangement selected for study ($D = C = T/2$, with a lid at the top of the vessel and thus no free surface), it might be reasonably expected that the structures above the impeller will be similar. Confirmation of this expectation via further measurements would aid utilization of MIs for optimization of the location of feed pipes to exploit the shorter mixing times encountered when feed insertion is made inside the MI vortex.[5] Further, the interaction of the trailing vortices with the MIs could also be exploited, as when the MI crosses a trailing vortex the superimposition of the locally higher energy levels from both structures might suggest a suitable location and instant for pulsed injection at a point within the MI. Similarly, it would be useful to apply similar approaches to process-specific vessel/impeller combinations so that the precise location, extent, frequency, and magnitude of the instabilities can be known *a priori* and exploited for mixing enhancement purposes.

Notwithstanding the above considerations, this work has provided confirmation that most, if not all, of the previously reported observations on MIs in PBT-stirred vessels are encountered in the present data. It was also shown that the complexity of the flow phenomena is such that the flow can appear chaotic or exhibit a multitude of frequencies that, in the particular flow geometry under study, are nevertheless dominated by the structures described above.

Acknowledgments

Financial support for the work reported here was provided by the Engineering and Physical Sciences Research Council (EPSRC) of the UK, grants EP/D032539 and EP/E055958.

Notation

Abbreviations

CFD = computational fluid dynamics
FFT = fast Fourier transforms
LDA = laser doppler anemometry
LOM = low order model
MI = macro instability
PBT = pitched blade turbine
PIV = particle image velocimeter
POD = proper orthogonal decomposition
RT = rushton turbine

Greek letters

λ_n = energy of the *n*th model (m^2s^{-2})
ϕ = Phase angle($\cdot$)
Φ_n = *n*th POD spatial eigenfunction (–)
$\omega_{\theta\mathrm{MI}}$ = Dimensional vorticity in the azimuthal plane associated to the MI (s^{-1})
$\omega_{\theta\mathrm{TV}}$ = Dimensional vorticity in the azimuthal plane associated to the trailing vortices (s^{-1})
ω_z = Dimensional vorticity in the vertical plane (s^{-1})

Roman letters

a_n = *n*th POD temporal eigenfunction (ms^{-1})
C = impeller clearance (m)
D = impeller diameter (m)
f = frequency (Hz)
f' = nondimensional frequency (–)
f'_{TV} = nondimensional precessional frequency associated to the trailing vortices (–)
J = magnitude of a velocity vector (ms^{-1})
N = impeller rotational speed(rps)
N_s = POD modes (–)
r = radial coordinate (m)

Re = reynolds number (−)
T = vessel diameter (m)
T_{imp} = period of impeller revolution (s)
T_{MI} = period of MI precession (s)
u' = fluctuating velocity (ms^{-1})
U = M=mean velocity (ms^{-1})
u = total velocity (ms^{-1})
u_θ = aztimuthal velocity componenet (ms^{-1})
u_{LOM} = velocity associate to the LOM (ms^{-1})
u_r = radial velocity component (ms^{-1})
V_{tip} = velocity of the tip of the blade (ms^{-1})
X,y = cartesion coordinate (m)
z = axial coordinate (m)

Literature Cited

1. Tatterson GB. *Scale-up and design of industrial mixing processes.* Mc Graw-Hill Inc., New York. 1994.
2. Assirelli M, Bujalski W, Eaglesham A, Nienow AW. Study of micromixing in a stirred tank using a Rushton turbine: Comparison of feed positions and other mixing devices. *Chem Eng Res Des.* 2002;80:855–863.
3. Ducci A, Yianneskis M. Direct determination of energy dissipation in stirred vessels with two-point lda. *AIChE J.* 2005;51:2133–2148.
4. Ducci A, Yianneskis M. Vortex identification methodology for feed insertion guidance in fluid mixing processes. *Chem Eng Res Des.* 2007;85:543–550.
5. Ducci A, Yianneskis M. Vortex tracking and mixing enhancement in stirred processes. *AIChE J.* 2007;53:305–315.
6. Larsson G, Tornkvist M, StahlWernersson E, Tragardh K, Noorman H, Enfos S. Substrate gradients in bioreactors: origin and consequences. *Bioprocess Eng.* 1996;14:281–289.
7. Winardi S, Nagase Y. Unstable phenomenon of flow in a mixing vessel with a marine propeller. *J Chem Eng Jpn.* 1991;24:243–249.
8. Bruha O, Fort I, Smolka P. Large scale unsteady phenomenon in a mixing vessel. *Acta Polytech Czech Tech Univ Prague.* 1993;27:33.
9. Montes J, Boison H, Fort I, Jahoda M. Velocity field macro-instabilities in an axially agitated mixing vessel. *Chem Eng J.* 1997;67:139–145.
10. Hasal P, Montes JL, Boisson HC, Fort I. Macro-instabilities of velocity field in stirred vessels: Detection and analysis. *Chem Eng Sci.* 2000;55:391–401.
11. Roussinova VT, Grgic B, Kresta S. Study of macro-instabilities in stirred vessel tanks using a velocity decomposition technique. *Chem Eng Res Des.* 2000;78:1040–1052.
12. Roussinova V, Kresta S, Weetman R. Low frequency macroinstabilities in a stirred tank: scale up and prediction based on large eddy simulations. *Chem Eng Sci.* 2003;58:2297–2311.
13. Roussinova V, Kresta S, Weetman R. Resonant geometries for circulation pattern macroinstabilities in a stirred tank. *AIChE J.* 2004;50:2986–3005.
14. Nikiforaki L, Montante G, Lee KC, Yianneskis M. On the origin, frequency and magnitude of macro-instabilities of the flows in stirred vessels. *Chem Eng Sci.* 2003;58:2937–2949.
15. Galletti C, Paglianti A, Lee KC, Yianneskis M. Reynolds number and impeller diameter effects on instabilities in stirred vessels. *AIChE J.* 2004;50:2050–2063.
16. Galletti C, Paglianti A, Yianneskis M. Observations on the significance of instabilities, turbulence and intermittent motions on fluid mixing processes in stirred reactors. *Chem Eng Sci.* 2004;60:2317–2331.
17. Hasal P, Jahoda M, Fort I. Macro-instability: a chaotic flow component in stirred tanks. *Phil Trans of the Royal Society A-Mathematical Phys Eng Sci.* 2008;366:409–418.
18. Roy S, Acharya S, Cloeter MD. Flow structure and the effect of macro-instabilities in a pitched blade stirred tank. *Chem Eng Sci.* 2010;65:3009–3024.
19. Ducci A, Doulgerakis Z, Yianneskis M. Decomposition of flow structures in stirred reactors and implications for mixing enhancement. *Ind Eng Chem Res.* 2008;47:3664–3676.
20. Doulgerakis Z, Yianneskis M, Ducci A. On the interaction of trailing and macro-instability vortices in a stirred vessel-enhanced energy levels and improved mixing potential. *Chem Eng Res Des.* 2009;87:412–420.
21. Sirovich L. Turbulence and the dynamics of coherent sturctures. *Quart Appl Math.* 1987;45:561–590.
22. Berkooz G, Holmes P, Lumley J. The proper orthogonal decomposition in the analysis of turbulent flows. *Ann Rev Fluid Mech.* 1993; 25:539–575.
23. van Oudheusden B, Scarano F, van Hinsberg N, Watt D. Phase-resolved characterization of vortex shedding in the near wake of a square-section cylinder at incidence. *Exp Fluids.* 2005;39:86–98.
24. Perrin R, Cid E, Cazin S, Sevrain A, Braza M, Moradei F, Harran G. Phase-averaged measurements of the turbulence properties in the near wake of a circular cylinder at high Reynolds number by 2c-piv and 3c-piv. *Exp Fluids.* 2007;42:93–109.
25. Tabib MV, Joshi JB. Analysis of dominant flow structures and their flow dynamics in chemical process equipment using snapshot proper orthogonal decomposition technique. *Chem Eng Sci.* 2008;63:3695–3715.
26. Moreau J, Line A. Proper orthogonal decomposition for the study of hydrodynamics in a mixing tank. *AIChE J.* 2006;52:2651–2655.
27. Bruha O, Fort I, Smolka P, Jahoda M. Experimental study of turbulent macroinstabilities in an agitated system with axial high-speed impeller and with radial baffles. *Collect Czech Chem Commun.* 1996;61:856–867.
28. Myers KJ, Ward RW, Bakker A. A digital particle image velocimetry investigation of flow field instabilities of axial-flow impellers. *Trans ASME, J Fluid Eng.* 1997;119:623–632.
29. Doulgerakis Z. Large scale vortex and strain dynamics in mixing vessels and implications for macro-mixing enhancement. Ph.D. thesis, King's College London, University of London, United Kingdom. 2010.
30. Schäfer M, Yianneskis M, Wächter, Durst F. Trailing vortices around a 45° pitched blade impeller. *AIChE J.* 1998;44:1233–1246.
31. Paglianti A, Montante G, Magelli F. Novel experiments and mechanistic model for macroinstabilities in stirred tanks. *AIChE J.* 2006; 52:426–437.
32. Jaworski Z, Dyster KN, Nienow AW. The effect of size, location and pumping direction of pitched blade turbine impellers on flow patterns: LDA measurements and CFD predictions. *Chem Eng Res Des.* 2001;79:887–894.

Manuscript received May 10, 2010, revision received Sept. 29, 2010, and final revision received Dec. 7, 2010.